AIAA AVIATION Forum
August 2-6, 2021, VIRTUAL EVENT
AIAA AVIATION 2021 FORUM

10.2514/6.2021-2471

Aerodynamic Optimization of Wing-Mounted Propeller Configurations for Distributed Electric Propulsion Architectures

Matthew A. Clarke*, Racheal M. Erhard†, and Juan J. Alonso ‡
Department of Aeronautics and Astronautics, Stanford University, Stanford CA, 94305

In this paper, we demonstrate the use of new capabilities in the SUAVE open-source design environment to optimize multi-propeller and multi-rotor aircraft. Departing from traditional single-point approaches, the design objective of minimizing total energy consumed over the entire mission profile guarantees arrival to a mission-level optima. This holistic approach to vehicle design serves to ensure that optimizations are not biased to one flight condition, making it particularly applicable in instances where the numerous flight profile segments are of comparable duration, as is the case of regional and urban air mobility. This study utilizes SUAVE's medium-fidelity aerodynamic analysis module that comprises semi-empirical and numerical models for analyzing propellers, rotors, lifting surfaces and their interactions. Methods are validated using wind tunnel data. We then examine three distinct aircraft configurations that are projected to facilitate future short-range commuter travel. Two of these aircraft possess distributed electric propulsion architectures, in which propulsors are situated around the airframe.

Nomenclature

b	=	wing span
c	=	section chord
$C_l(y)$	=	sectional lift coefficient
C_L	=	lift coefficient
$\overline{c}_l$	=	average lift coefficient
$C_{m,n}$	=	wing influence coefficient matrix
C_n	=	normal force coefficient
$C_{r,t}$	=	propeller wake influence coefficient matrix
C_D	=	drag coefficient
C_{Di}	=	induced drag coefficient
C_P	=	power coefficient
C_T	=	thrust coefficient
E	=	battery energy
J	=	advance ratio
L/D	=	lift-to-drag ratio
n	=	quantity of component
r	=	radial location
R	=	propeller/rotor radius
S_{ref}	=	wing reference area
t	=	time
T_{design}	=	propeller design thrust
$TOGW$	=	takeoff gross weight
V_{design}	=	propeller design velocity
WMA	=	wing-mounted angle
y	=	spanwise location
α	=	aircraft angle of attack
$\boldsymbol{\beta}$	=	blade twist distribution
β_{75}	=	blade pitch at 75% chord
β_c	=	blade pitch command
ΔC_p	=	surface pressure coefficient difference ($C_{P_{lower}} - C_{P_{upper}}$)
η	=	propeller efficiency
Γ	=	circulation
λ	=	taper ratio
$\boldsymbol{\theta}$	=	wing twist distribution

Subscripts

EOF	=	end of flight
max	=	maximum
m	=	motor
$prop$	=	propeller
rot	=	rotor
tot	=	rotor

*Ph.D. Candidate, Department of Aeronautics and Astronautics, AIAA Student Member
†Ph.D. Candidate, Department of Aeronautics and Astronautics, AIAA Student Member
‡Professor, Department of Aeronautics and Astronautics, AIAA Fellow

I. Introduction

The surge of interest in all-electric regional and urban air mobility has led to an increased need for understanding interference effects prominent in propeller-driven aircraft. The aerodynamic interactions between propeller wakes and lifting surfaces can be leveraged to achieve improved aircraft performance, particularly among distributed electric propulsion (DEP) aircraft configurations. A revisiting of counter-rotating and advanced prop-fan systems with open rotors has further accentuated the need to comprehend these interactions. Recent experiments by Sinnige et al. [1] demonstrate that for configurations with up-inboard rotating propellers, swirl in the propeller slipstream lessens the effect of wingtip vortices, leading to an increase in wing lift. These findings corroborate numerous numerical and analytical results found in the literature [2–6]. In other studies, McVeigh et al. [7] and Stone [8] coupled the induced velocities from separate implementations of the blade element momentum theory (BEMT) to a modified lifting-line model and fixed-wake panel model of the wing respectively. The mutual interaction between the wing and propeller was however neglected in these two approaches. Veldhuis [9] accounted for this inter-dependence using a vortex-lattice method (VLM) approach to model both the propeller and the wing, demonstrating close agreement with experimental tests.

Higher-fidelity models that remove the inviscid and irrotational assumption have also been studied in [10–14]. Although such approaches have the potential to capture some of the underlying flow properties arising from propeller–wing interaction, the computational cost associated with mesh generation, large matrix inversion to solve for state variables, and post-processing makes it intractable for early stage and iterative conceptual design. The development of computational tools sufficiently accurate to provide reliable estimates of vehicle performance, but fast enough to enable iterative design and geometric optimization of the aircraft is therefore necessary. Structural loads, acoustic noise footprint and aircraft stability are also strongly coupled with these interactions, underscoring the need for tools that capture interference effects. As a result, medium-fidelity approaches have come to the forefront in the design of non-conventional vehicles, such as electric vertical takeoff and landing (EVTOL) aircraft configurations.

In this paper, we lay the foundation for interdisciplinary studies by first providing a thorough review of vehicle optimization over a full flight profile. The remainder of this paper is broken down into eight sections. Section II provides an overview of the aircraft modeled in this current study. This is followed by a description of the analytical methods in Section III and a validation using recent experimental work in Section IV. Section V provides an assessment of the baseline aircraft and a discussion on the impact of propeller rotation on aerodynamic performance, while Section VI details the flight profile over which each aircraft is to be optimized. The optimization problem is described in Section VII and a summary of the results is presented in Section VIII.

II. Baseline Aircraft Models

An overview of configuration and sub-system components for the three aircraft studied in this paper is presented below. These aircraft are designed to carry a maximum capacity of 4 passengers. The first vehicle is an electric general aviation (GA) aircraft, modeled after Modification II of the NASA X-57 experimental aircraft. This aircraft is denoted GA-2P in this study. The second aircraft possess the same fuselage and lifting surfaces as the GA-2P but has 8 smaller 5-bladed propellers that create a more continuous blown-wing effect along the span of the wing. Correspondingly, the model is denoted GA-8P. The third aircraft is a tandem tilt-wing (TTW) EVTOL aircraft, with wings of equivalent span and aspect ratio. The wings are also vertically offset, with four rotors mounted on each wing. Renderings of the three vehicles are provided in Figure 1. Here, propellers and rotors are numbered for future reference in the following sections of the paper. Parametric data describing the attributes of the baseline models are documented in Table 1.

The major aircraft components including wings, batteries, rotors, motors and fuselages are defined in SUAVE as physical component classes with mass attributes such as center-of-gravity and moment of inertia, geometric attributes unique to the respective component, and in special cases, functions that characterize simulated operation. Structural components for bearing loads such as booms and fuselage bulkheads are subsequently sized using the physics-based weight build-up method implemented within the code [15]. The motor model used in this study is a brushed AC motor that assumes no loss in latency from switching signs as the internal commutator brushes keep the magnetic fields aligned in the desired phase with the magnets. Additionally, it is assumed that all motors of a particular aircraft are identical and electrically connected in parallel. This implies that these motors experience equivalent voltage and current profiles, further indicating that they are identically throttled. The Python-based SUAVE code also facilitates the optimization routines performed in this study through wrappers for both gradient and non-gradient-based optimization packages. As a result, the entire iterative design loop is self-contained within one code platform. Interactions between propeller or rotor wakes and lofted-body geometries such as the fuselage and booms are not considered in the present study.

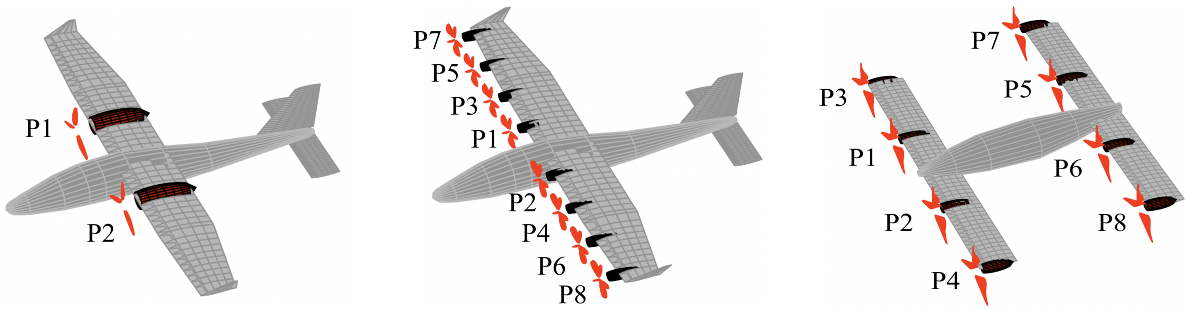

(a) GA-2P aircraft (b) GA-8P aircraft (c) TTW EVTOL aircraft

Fig. 1 DEP aircraft models.

Table 1 Vehicle Configuration Parameters

	GA-2P	GA-8P	TTW
		General Characteristics	
Capacity (pass.)	4	4	4
Length (m)	8.28	8.28	6.1
Wingspan (m)	11.4	11.4	9.6
Reference Area (m^2)	14.76	14.76	21.7
TOGW (lb)	3549	3622	4850
Battery Capacity (MW-hr)	0.444 $120s \times 80p$	0.444 $120s \times 80p$	0.828 $150s \times 120p$
Powerplant	2 3-bladed propellers w/ 52.7 kW motors	8 5-bladed propellers w/ 25.19 kW motors	8 3-bladed rotors w/ 100 kW motors
Propeller/Rotor Diameter (m)	1.94	1.16	2.4
		Performance	
Cruise Speed (mph)	175	175	175
Maximum Operational Altitude (ft)	14000	14000	5000

III. Computational Analyses

Documented in this section is the synergy of the medium-fidelity methods used to ascertain aerodynamic loads and performance. This includes a BEMT with an airfoil post-stall model to predict propeller aerodynamics and a quasi-steady propeller wake model using distributed vortex ring elements coupled with a VLM to predict wing performance in the presence of a propeller slipstream.

A. Wing and Lifting Surface Model

The VLM implementation, based on VORLAX [16], is used to compute aerodynamic loads on the wings and fuselage, modeled as a combination of flat surfaces. These surfaces follow the curvature of the camber line in the case of wings. Each surface is discretized into panels consisting of a horseshoe vortex with trailing legs that extend to infinity and a bound vortex at the quarter chord location. An example of this lattice is depicted in Figure 2a. The control point where aerodynamic loads are computed is located at the three-quarter chord of each panel. Velocities induced at this point by a vortex element are computed using the Biot-Savart law. If we let C represent the curve of a vortex filament of constant circulation Γ, the velocity due to the filament is obtained as

$$\vec{v} = \frac{\Gamma}{4\pi}\int_C \frac{dl \times \vec{r}}{r^3}. \tag{1}$$

For a straight line vortex filament, as shown in Figure 2b, the velocity induced at the control point P along the filament from point A to point B is

$$\vec{v}_{A,B} = \frac{\Gamma}{4\pi} \frac{\vec{r}_1 \times \vec{r}_2}{|\vec{r}_1 \times \vec{r}_2|^2} \vec{r}_0 \cdot \left(\frac{\vec{r}_1}{|\vec{r}_1|} - \frac{\vec{r}_2}{|\vec{r}_2|} \right), \tag{2}$$

where

$$|\vec{r}_0| = \sqrt{(x_2 - x_1)^2 + (y_2 - y_1)^2 + (z_2 - z_1)^2} \tag{3a}$$

$$|\vec{r}_1| = \sqrt{(x_p - x_1)^2 + (y_p - y_1)^2 + (z_p - z_1)^2} \tag{3b}$$

$$|\vec{r}_2| = \sqrt{(x_p - x_2)^2 + (y_p - y_2)^2 + (z_p - z_2)^2}. \tag{3c}$$

The approach to creating an aerodynamic coefficient matrix and applying flow tangency boundary conditions to compute circulation strength, and subsequently lift and induced drag of an entire vehicle, is well documented in [17] and [18]. The authors have therefore chosen not to further elaborate on the details regarding implementation but point the reader to the corresponding texts.

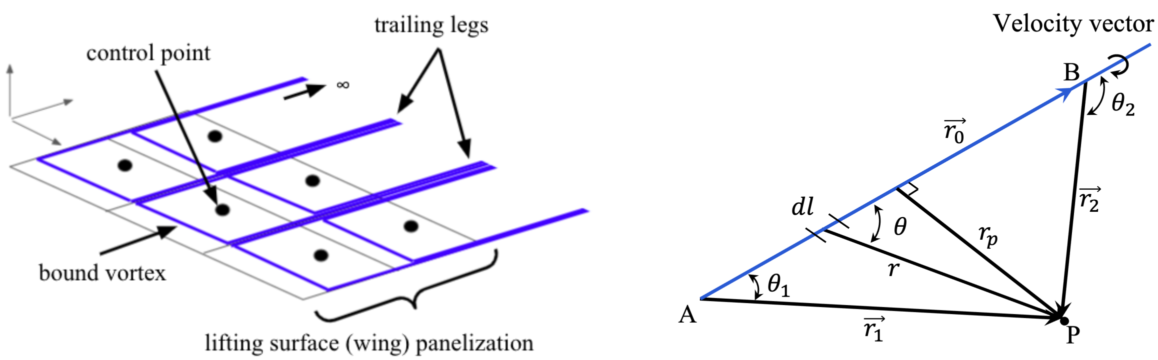

(a) Representative wing panels, trailing vortices and control points used in the SUAVE-VLM.

(b) Nomenclature for calculating the velocity induced by a finite-length vortex filament [18].

Fig. 2 Vortex lattice and filament notations.

B. Propeller and Helical Fixed-Wake Model

The BEMT model used for propeller and rotor analysis in SUAVE discretizes the blades into radial sections, each acting as quasi-2D airfoils. The two-dimensional characteristics of each section are evaluated at the local Reynolds number by way of a pre-computed surrogate model, constructed using data obtained from XFOIL [19] at a range of appropriate Reynolds numbers. This is supplemented with a post-stall airfoil model based on the semi-empirical approach developed by Spera [20] that calculates lift and drag coefficients at stalled regions of the rotating airfoils. Additionally, a Prandtl tip loss factor is applied to account for 3D effects along with a Prandtl-Glauert correction to account for compressibility effects. In this approach, the momentum theory of lift is equated with the circulation at the blade, and an iterative solver is used to equate the effective circulation in the wake to that at the blade. A Newton iteration is employed to converge on the inflow velocity profile at the plane of the rotating blades. This resulting model provides a good approximation of thrust, torque, and induced axial and tangential flows on the propeller or rotor blade.

Though the BEMT is suitable for estimating propeller performance, momentum theory lacks accuracy in the slipstream resolution when considering the wake interaction with downstream lifting surfaces. In such a case, a more realistic wake model is required. This has been established in SUAVE through the implementation of a helical fixed-wake (HFW) model based on potential flow theory. This approach models the wake as distributed vortex elements (DVE) or rings, and was also used by Patterson et al. [21]. As the propeller rotates about its axis at predefined time steps, vorticity is shed from the blade into the wake and is modeled by these vortex ring elements. By extending the total elapsed shed time of the wake to encompass the first few rotations where the helical profile can be assumed to be well-structured, the shape of the near field wake can be constructed. The vortex strength of each ring depends on the circulation at the blade element when it is shed, which is in turn dependent on the inflow to the propeller. Compared to fully resolved relaxed-wake models, fixed wake models suffer from small inaccuracies due to the non-converged nature of the solution. However, they balance the desire for higher accuracy and required computational cost when it comes to a more detailed representation of the slipstream, making it attractive for full flight profile simulations and optimization.

The HFW approach of representing vorticity as rings closely follows Helmholtz Vortex theorems which state that the strength of a vortex filament is constant and cannot end in a fluid but must either end at a boundary, extend to infinity, or, as in this case, form a closed loop. With a method that uses the same singularities as the horseshoe vortices of the VLM, the induced velocities generated by the potential of the propeller wake can be computed anywhere in the flow field. The vortex ring elements are planar and quadrilateral in shape, and consist of a bounded vortex filament of equal strength on all four sides. The total velocity induced by each ring can be computed in a similar manner as described in the VLM by summing the influence of the four individual ring filaments. If the vortex segment connects points A and B, the velocity at an arbitrary point p can be obtained from Equation 2. Therefore, the vortex ring induced velocity is

$$\vec{v}_{ring} = \vec{v}_{AB} + \vec{v}_{BC} + \vec{v}_{CD} + \vec{v}_{DA}. \tag{4}$$

Note that continuity of the vortex ring is preserved by the order of the subscripts, which indicate the direction of the circulation vector. The total induced velocity at a control point on the wing, denoted m, can be determined by numerically integrating the influence from the system of vortex rings and adding it to the influences induced by the system of horseshoe vortices on the wing,

$$\vec{v}_{tot_m} = \vec{v}_{wing_i} + \vec{v}_{wake_i}, \tag{5}$$

where

$$\vec{v}_{wing_m} = \sum_{n=1}^{N} \vec{C}_{m,n}\Gamma_n \tag{6a}$$

$$\vec{v}_{wake_m} = \sum \vec{C}_{r,t}\Gamma_r. \tag{6b}$$

Here, N is the total number of control panels on the lifting surface, and $C_{m,n}$ is the influence coefficient matrix, which depends on the geometry of the n^{th} horseshoe vortex and its distance from the control point of the m^{th} panel. The construction of these matrices for the VLM is outlined in [17]. Similarly, $C_{r,t}$ is the influence matrix constructed for the vortex ring system based on initial radial location, r, and the time step, t.

IV. Validation of Computational Methods

A. Validation of Isolated Propeller Performance Model

The BEMT model was validated against several test propellers throughout a range of operating conditions. The multitude of wind tunnel data available for the APC model propellers, as well as for the SR2 propeller, led to the selection of the APC 10x7 thin electric, APC 19x12 thin electric, and SR2 propellers for this validation study. The APC propellers have a fixed pitch, with geometry descriptions provided in Figure 13 in Appendix X.A. Each APC propeller was simulated throughout a range of advance ratios at a fixed angular rotation rate. The performance predicted from the BEMT is compared to wind tunnel results obtained by Brandt et al. [22], as shown in Figure 3. Here it is clear that the model tracks the thrust and power coefficients fairly well across a range of advance ratios. Slight differences in the power and thrust coefficients lead to optimistic propulsive efficiencies, however these results are still quite reasonable, with less than 10% error for advance ratios up to 0.7.

A similar validation study was conducted on the SR2 propeller geometry at a fixed freestream Mach number of 0.2. The SR2 propeller has variable pitch capability and thus was simulated for a range of blade pitch angles measured from the 75% radial location. The power coefficients and propulsive efficiencies predicted from these simulations are compared with wind tunnel results found by Stefko and Jeracki [23] in Figure 4. Similar accuracy in the power coefficients and propulsive efficiencies were found across a wide range of advance ratios and blade pitch angles. However, in comparing experimental data to the performance of the SR2 propeller simulated in SUAVE, two critical observations were made. The first concerns the poor numerical convergence resulting in non-smooth behavior of

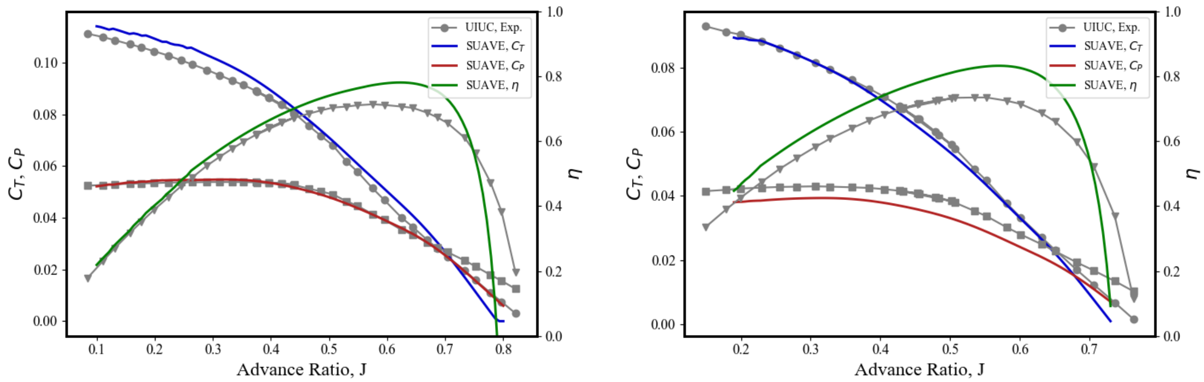

(a) APC 10x7 thin electric propeller performance. **(b) APC 19x12 thin electric propeller performance.**

Fig. 3 Validation of SUAVE BEMT on APC thin electric propellers.

propeller performance as a function of advance ratio J. The current implementation of the BEMT uses a Newton method iterative scheme to resolve the components of the induced velocities. Future work will provide a more robust convergence in which backward propagated gradients computed using an automatic differentiation package can be directly leveraged. The second and more noticeable difference is the reduced accuracy at low advance ratios, which becomes particularly divergent with increasing blade pitch. This divergence from the experimental results is indicative of the model's inability to truly capture stall effects, even with the post-stall model previously described. Despite these behaviors, the BEMT model is certainly appropriate for modeling propellers over a large subset of operating conditions and has proven acceptable for predicting the performance of propellers and rotors in conceptual design.

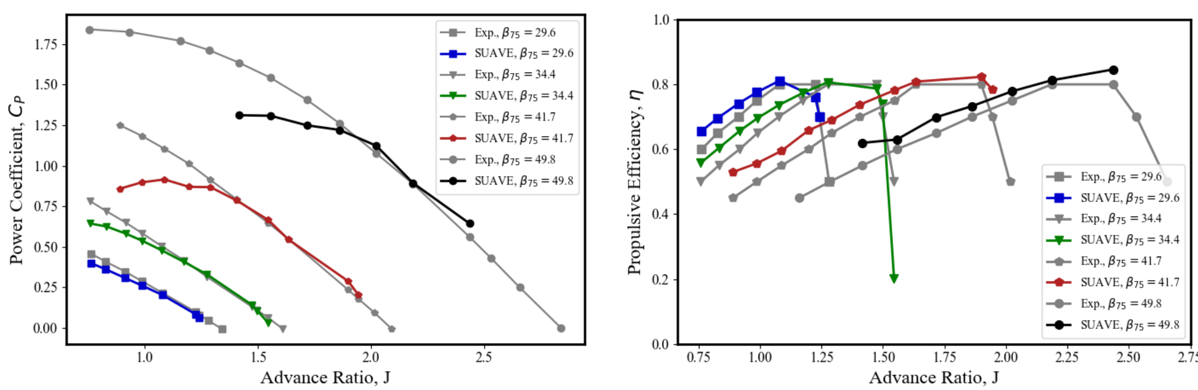

(a) SR2 propeller power coefficient. **(b) SR2 propeller efficiency.**

Fig. 4 Validation of SUAVE BEMT on SR2 propeller.

B. Validation of Propeller Wake-Wing Interaction

The propeller wake-wing interaction analysis is validated through comparison to experimental wind tunnel data produced by Veldhuis [24], who explored the interaction effect of a simple propeller-wing system with a 5.33 aspect ratio rectangular wing and a propeller diameter of 0.236m. The geometry and conditions from the experiments were reproduced in SUAVE, with a chord-based Reynolds number of 8e5, a freestream Mach number of 0.15, and a propeller advance ratio of 0.85. Figure 5a shows the model in SUAVE, and Figure 5b shows the lift distribution on the wing in the presence of the propeller wake at an angle of attack of 4°. The spanwise distribution of normal force coefficients for the clean wing, as well as the inboard-up and outboard-up rotations with the propeller included, are shown in Figure 6.

From these results, it is clear that the fixed helical wake is properly capturing the trends in aerodynamic loading, and is particularly accurate for low angles of attack. For the 10° simulation, the results diverge slightly from the experimental data for both the clean wing and propeller interaction simulations. The slight over-prediction of lift on the clean wing for this test case is attributed to separation effects along the wing that are not captured in the VLM. Additional discrepancies in the general shape of the lift distribution for the 10° case with propeller interaction are likely an indicator that the helical fixed-wake assumption is beginning to break down. In this case, the true propeller wake is not appropriately modeled under the axisymmetric wake assumption. Despite this finding, the wake model is quite accurate at a range of reasonable angles of attack and is an efficient solution that enables rapid analysis of the propeller-wing interaction.

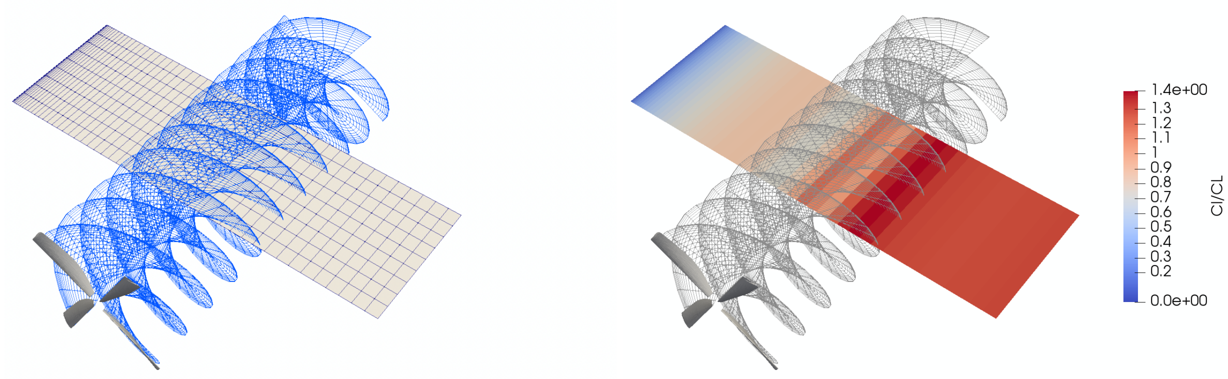

(a) Propeller and wing model in SUAVE. **(b) Normalized lift distribution along wing.**

Fig. 5 Propeller and wing modeled in SUAVE for a test case at α = 4°.

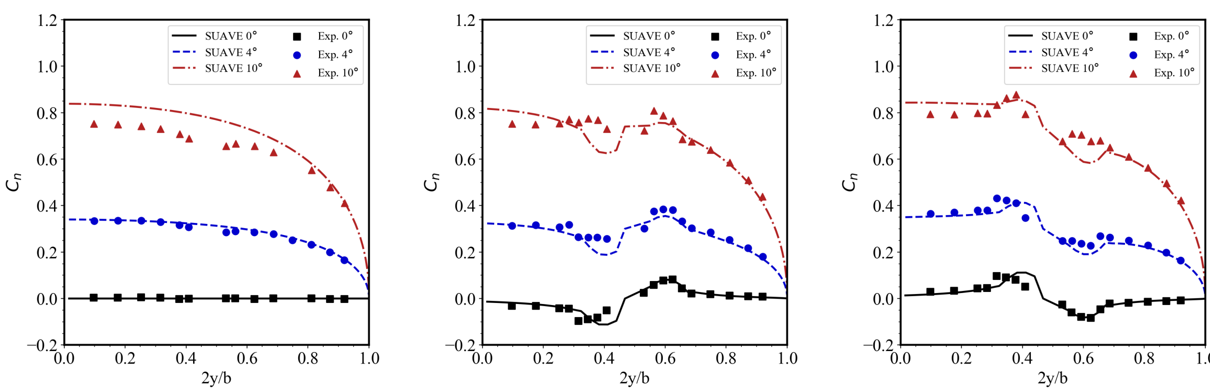

(a) Clean wing. **(b) Outboard-up rotation.** **(c) Inboard-up rotation.**

Fig. 6 Propeller-wing validation, as compared to wind tunnel data from Veldhuis [24].

V. Aerodynamic Results for Baseline Aircraft Models

The approaches detailed in this paper demonstrate how a systems-level tool can assess the impact of component interactions, notably between propulsion networks and lifting surfaces. Shown in Figure 7a is a model of the lifting surfaces, propellers, nacelles and fuselage of the GA-2P aircraft, along with a visualization of the first few revolutions of the helical fixed wakes of the propellers. The two propellers maintain an outboard-up rotation in this example. Figure 7b shows the corresponding difference in surface pressure between the lower and upper wing surfaces at a 3° angle of attack. Noticeable features of this pressure distribution include higher pressure differences near the leading edge as well as regions of the main wing that experience local changes in velocity due to the axial and tangential velocity components of the propeller wakes. The center-line of the propeller axes are demarcated as the red lines in Figure 7b. On the wing section outboard of the propeller, where blades advance from beneath the wing, the local wing section experiences an increase in the effective angle of attack due to the induced upwash from the blades. This leads to increased local lift and correspondingly a larger ΔC_P. The opposite trend can be seen in the wing section inboard from the propellers.

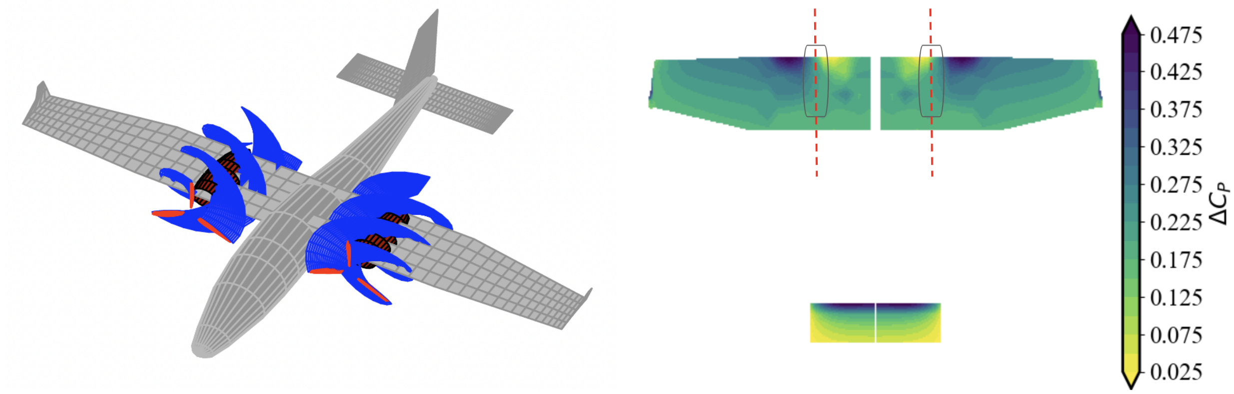

(a) Representation of aircraft surfaces and propeller wakes of aerodynamic analysis.

(b) Differential pressure on wing surfaces.

Fig. 7 Twin-engine VLM panel representation and ΔC_P distribution

The influence of the wake-wing interaction on wing loading for the three baseline aircraft described in Section II is next explored. Various propeller rotations and their effect on wing loading at a fixed wing angle of attack of 3° are compared. The GA-2P and TTW aircraft are tested with fixed advance ratios of 1 for each propeller, while the GA-8P, with propellers of much smaller diameter, is tested with an advance ratio of 1.5 to provide a more realistic rotation rate.

GA-2P Spanwise Loading Comparisons

Figure 8 portrays the spanwise lift distribution of the GA-2P for two cases with opposing propeller rotations. The resulting lift and drag coefficients of each test case are provided above each figure. The loading on the main wing is as expected, with the inboard-up rotation of Case 1 increasing the sectional lift near the fuselage while reducing sectional lift near the outboard sections, shown in Figure 8a. The opposite trends hold for the outboard-up propeller rotations of Case 2, shown in Figure 8b. The increased sectional lift near the wing center in Case 1 leads to increased downwash from the main wing incident on the horizontal tail, causing a reduction in effective tail angle and resulting in a reduction in spanwise lift when compared to the outboard-up rotation. This is shown by the red curves in Figure 8.

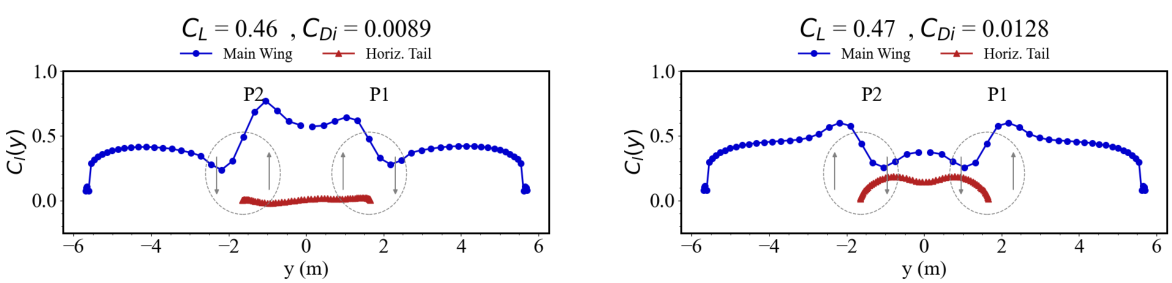

(a) Case 1: All inboard-up rotation.

(b) Case 2: All outboard-up rotation.

Fig. 8 Spanwise lift distribution of GA-2P.

GA-8P Spanwise Loading Comparisons

The spanwise loading of the GA-8P aircraft is shown in Figure 9 for four combinations of propeller rotation directions. Case 1, with all inboard-up propeller rotations, is shown in Figure 9a while Case 2 maintains all propellers with outboard-up rotation in Figure 9b. Figures 9c and 9d correspond to alternating rotating propellers. In 9c, the wingtip propellers rotate in such a way that opposes the wake roll-up, whereas in 9d the rotation further accentuates the roll-up, otherwise viewed as the vorticity, of the wake. It can be inferred from these plots that the configuration with the highest L/D ratio is that in which all propellers act to reduce the strength of the wingtip vortex, that is, Case 1. This corroborates the findings by Sinnige et al. [1], which experimentally demonstrated that the swirl of inboard-up rotating wingtip mounted propellers partially cancels the swirl associated with the wingtip vortex, leading to a reduction in induced drag. That said, the small differences in drag coefficient of the four cases studied here confirm the findings by Jameson [25] that for closely spaced propellers, such as those of this configuration, the slipstreams can be said to act in similar manner to a continuous jet-stream that increases the local velocity of the wing almost uniformly.

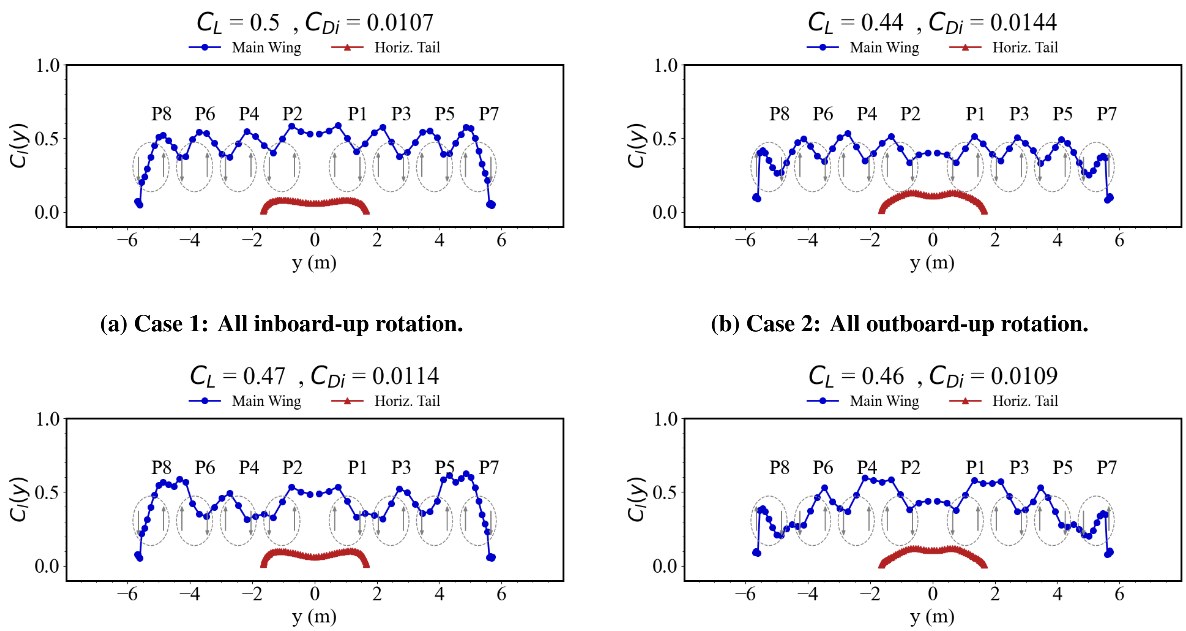

(a) Case 1: All inboard-up rotation.

(b) Case 2: All outboard-up rotation.

(c) Case 3: Alternating rotation.

(d) Case 4: Alternating rotation.

Fig. 9 Spanwise lift distribution of GA-8P.

TTW Spanwise Loading Comparisons

Figures 10a and 10b show the wing loading for the TTW aircraft with all inboard-up and all outboard-up rotating rotors, respectively. Figure 10c corresponds to the configuration with rotors adjacent to the fuselage rotating inboard-up and wingtip mounted rotors rotating outboard-up while Figure 10d depicts the reverse, where the four inner-most rotors are rotating outboard-up while the wingtip mounted rotors rotate inboard-up. The effect of the blade rotation on loading, particularly at the wingtip, can be differentiated in these plots whereby configurations with inboard-up rotating wingtip rotors result in an increase in C_l near the wingtip as seen in Cases 1 and 4. Higher sectional lift coefficients of these two cases compared to Cases 2 and 3, where tip-mounted rotors promote wingtip swirl, does however come with a certain structural drawback. Though not addressed in this paper, the impact of blade rotation on lift distribution is correlated to the magnitude of bending moment at the root of the wing. As a result, aircraft designers should couple disciplines when seeking to size load-bearing structures in the wing along with the center wingbox.

VI. Mission Setup

The flight profiles are made up of a series of mission segments, each representing the kinematics of the vehicle, such as cruise, accelerating climb, or descent. These segments are made utilizing a pseudospectral collocation method based upon the formation of generic differentiation and integration matrices for a given number of control points in a mission made up by joining individual flight segments [26]. In this paper, we look at expanding the control points themselves to

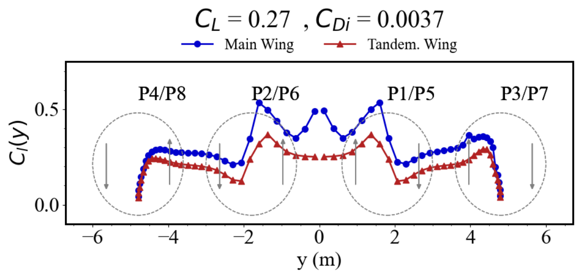

(a) Case 1: All inboard-up rotation.

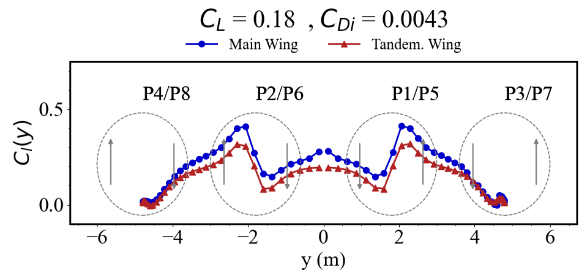

(b) Case 2: All outboard-up rotation.

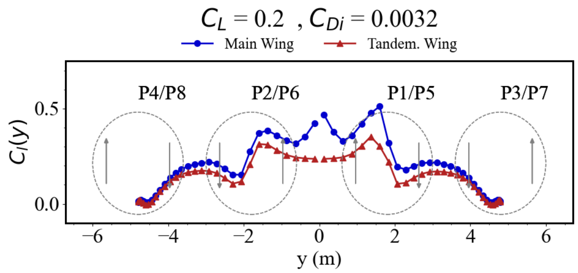

(c) Case 3: Alternating rotation.

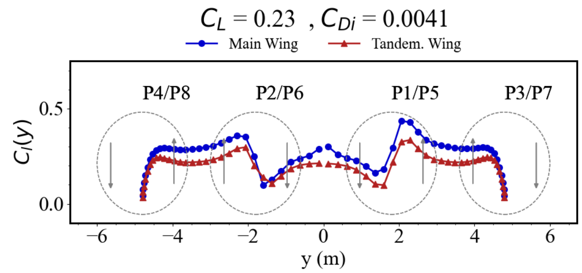

(d) Case 4: Alternating rotation.

Fig. 10 Spanwise lift distribution of tandem tilting-wing EVTOL.

look at snapshots of the time-varying load on the wing due to the inclusion of propeller wakes. This will be discussed in more detail later in this section.

The simulation of entire missions, as opposed to single design points, permits a more holistic understanding of aircraft performance. Through such an approach, the now-informed designer can leverage peripheral information to construct better-posed optimization problems. The mission is numerically solved by determining the forces on the aircraft as well as the required angle of attack relative to the freestream and the required throttle settings of the propulsion system needed to achieve the kinematics describing the flight profile. Examples of vehicle motion are a constant speed at a constant altitude, a linear climb rate between two defined altitudes, and aircraft deceleration at a constant speed with a linear pitch rate. A summary of the mission segments for each vehicle is documented in Table 2. A more detailed description of the parameters characterizing each flight segment is provided in Table 5 in the Appendix. This includes a breakdown of the altitude, speed and acceleration simulated for each mission segment. The premise of SUAVE to give the user full autonomy in specifying a mission means that attention must be made when defining segment properties to realistic missions also documented in the Appendix (see Table 5). This is achieved by ensuring that the initial condition of any particular segment is equivalent to the final conditions of the preceding segment.

These flight profiles were designed to be representative of the typical missions which these aircraft would perform during standard service operation. This implied that they conform to service ceilings, maximum speeds and allowable climb rates documented in 14 CFR §23. This section of the Code of Federal Regulation documents airworthiness standards for general aviation airplanes weighing less than 19,000 pounds with 19 or fewer seats. On the other hand, the flight profile of the EVTOL aircraft was designed to meet criteria within certain parts of 14 CFR §23, 14 CFR §27 for rotorcraft, along with the relatively new 14 CFR §135 for the emerging commuter and on-demand aircraft. A cruising altitude of 2500 feet is chosen to reflect regional and urban air mobility in Class B, C, and E airspace. These two flight profiles are depicted in Figure 11.

VII. Optimization Formulation

The baseline geometries for the three aircraft established in Section II were simulated over the corresponding mission profiles discussed in Section VI, with SUAVE's mission solver converging on the appropriate propeller angular rates, throttle, and wing angle of attack for each flight segment. The direction of rotation for all three aircraft are of Case 1

Table 2 Aircraft Flight Segments

Segment	GA	TTW
1	Takeoff (TO)	Vertical Climb (VC)
2	Departure End of Runway (DER)	Vertical Transition (VT)
3	Initial Climb Area (ICA)	Climb Transition No. 1 (CT)
4	Climb (CL)	Climb Transition No. 2 (CT)
5	Cruise(CR)	Climb (CL)
6	Descent (D)	Cruise (CR)
7	Downleg (DL)	Descent (D)
11	Baseleg (BL)	Approach Transition (AT)
12	Final Approach (FA)	Descent Transition (DT)
13	Landing (L)	Vertical Descent (VD)
14	Reverse Thrust (RT)	-

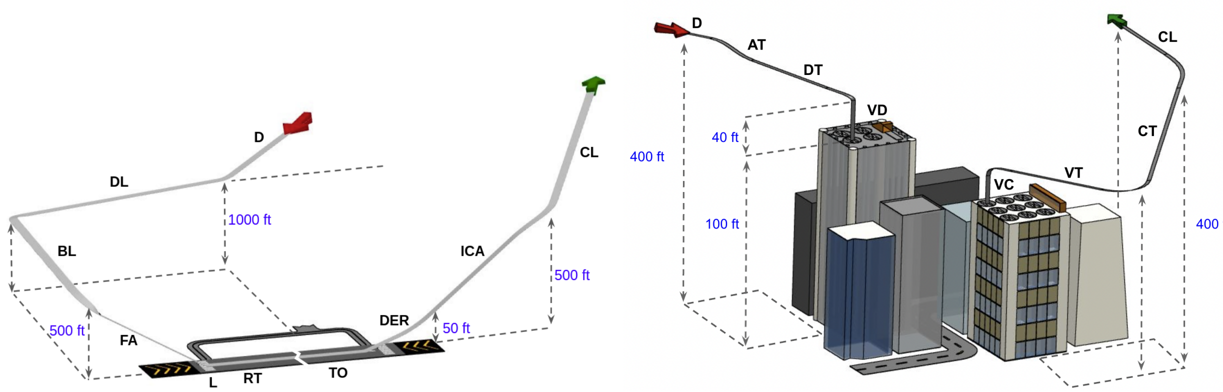

(a) Flight profile of GA aircraft **(b) Flight profile of EVTOL aircraft.**

Fig. 11 Flight profile diagrams.

convention, where all blades rotate in an inboard-up fashion. The resulting energy consumption is used as a benchmark for the following vehicle optimization studies, with the objective of minimizing the total expended energy over the entire mission. The design variables include both propeller and wing geometries and parameters. The propeller blades, often consisting of 15 or more radial stations to facilitate the convergence of the Newton solver in the BEMT, can account for upwards of 60 design variables when considering blade twist, chord, thickness, and sweep along the blade. To reduce this number of propeller design variables, three approaches are recommended: 1) creating coarse blades with fewer design variables and interpolating between stations to ensure a sufficient number of stations is provided for convergence, 2) representing blade variables as continuous functions such as polynomials or b-splines that can be defined using fewer variables, or 3) using an intermediary step that allows the propeller to be defined by desired performance characteristics such as tip radius, design thrust or torque, airspeed, rpm, and average lift coefficient. This last approach is adopted in this study, whereby the methodology developed by Adkins and Liebeck [27] for designing propellers with minimum induced power losses is adapted to handle large inflow angles, as well as the inclusion of sectional airfoil data that accounts for compressibility and skin friction drag. The hub fraction is held constant at 12% of the propeller tip.

Wing geometry in SUAVE can range from a simple trapezoidal planform parameterized by wing area, aspect ratio, sweep, dihedral and twist at the root and tip, to more detailed parameterizations that include information about segmented wings with sectional twist, camber, and control surface deflection. We leveraged this hierarchy of parametric detail to reduce the number of design variables of the optimization problem and accelerate function evaluations within the optimizer. Shown in Figure 12 is the annotated wing of the GA aircraft with some of the major parameters denoted. Here, the chords at each section are defined as a percentage of the root chord. Therefore, by keeping a constant wing area and changing taper, we can update the entire planform of the wing proportionately.

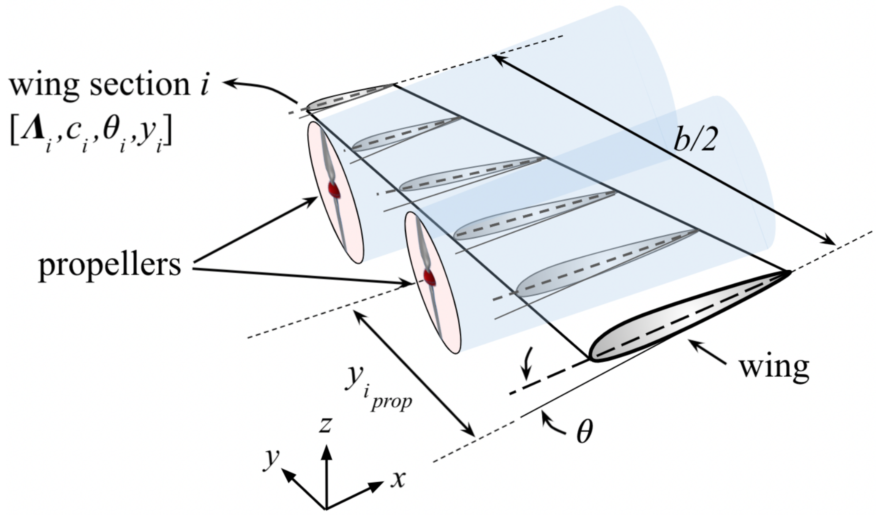

Fig. 12 Wing geometry parameterization.

The combined propeller-wing optimization formulation for this problem is given as

$$
\begin{aligned}
\textit{minimize} \quad & E_{EOF} \\
\textit{w.r.t.} \quad & [\boldsymbol{c}, \boldsymbol{\beta}, \boldsymbol{t}] = f\left(V_{design}, R_{tip}, T_{design}, \overline{c}_l\right), b, \lambda, \boldsymbol{\theta}, y_{i_{prop}} \\
\textit{subject to} \quad & M_{tip} \le M_{max} \\
& R_{tip} \le R_{max} \\
& S_{ref} = const.
\end{aligned}
\tag{7}
$$

where b is the wingspan, λ is the taper ratio of the wing, $\boldsymbol{\theta}$ is a vector of sectional twists of the wing and $y_{i_{prop}}$ is the location of the i^{th} propeller or rotor, given as percentage of total span. The wing planform area, S_{ref}, remains unchanged from the baseline configuration. E_{EOF} is the total energy at end-of-flight, otherwise referred to as the total integrated power consumption throughout the mission. T_{design}, V_{design}, and $\overline{c}_l$ are the design thrust, design velocity, and average lift coefficient along the blade. These variables are used to generate the optimal propeller blade geometry. The tip radius is explicitly constrained by a maximum radius, R_{max}, that prevents overlap between propellers, and is also implicitly constrained by a maximum tip Mach number for noise reduction. The percent spanwise location of the propellers of GA-8P were held fixed to keep them equidistant along the span of the wing. The ethos behind optimizing sectional wing parameters rather than conducting a topology optimization, as suggested by Chauhan and Martins [28], lies in the realistic cost that would be associated with manufacturing deformed planforms using tools in existence today.

VIII. Optimization Results

The initial and optimized values of the design variables for each aircraft configuration are compared in Table 3. The corresponding energy consumption and percent reduction over the respective flight profiles are also documented above the geometric parameterizations. In this table, the term "Propeller" is used in reference to both propellers and rotors depending on the configuration for brevity. Propeller numbers in rows 8-11 refer to their locations on the respective aircraft as shown in Figure 1.

Starting with the GA-2P aircraft, a 5% reduction in total battery energy is realized after optimization. By accounting for vehicle performance over the entire flight profile, that is with the inclusion of the various climb segments and phases of vehicle descent, we arrive at an optimized aircraft with a 13% increase in wingspan, indicating an increased aspect ratio given that wing area is held constant. This comes in conjunction with optimized propellers designed at a 17% higher thrust and a slightly lower design speed. Propeller radius increases from 0.96 m to 1.12m. This design value can be attributed to the 0.6 tip Mach active constraint. Also observed is the increase in spanwise location of the propellers. This outward movement of propellers was anticipated since the action of an inboard-up rotating propeller reduces the strength of the wingtip vortex, thus lowering induced drag. However, it can be noticed that the propellers do not approach the upper bound of the wingtip location. A reason for this may be due to the fact that the chord becomes smaller near the wingtip, with a taper ratio of 0.54 in the optimized case. Therefore, the closer the propeller is to the fuselage, the more wing area it is effectively blowing, leading to a lower required wing angle and associated induced drag for each mission segment. In this case, the balance between reducing wingtip induced swirl, and increasing local lift near the higher-chord regions of the wing places the optimal propeller at the 34% span location.

Table 3 Summary of Vehicle Optimization.

	GA-2P		**GA-8P**		**TTW**	
	Initial	Optimized	Initial	Optimized	Initial	Optimized
Battery Energy (KWhr)	61.01	57.96	40.51	37.57	114.77	103.84
Percent Reduction	-	5.00	-	7.25	-	9.52
Design Variable						
Propeller Design Thrust (N)	900.00	1059.59	350.00	376.82	5395.50	5573.87
Propeller Design Speed (mph)	135.00	119.04	130.00	138.58	22.36	18.253
Propeller Tip Radius (m)	0.97	1.12	0.58*	0.55	1.20	1.38
Propeller 1/2 % Span Location	0.23	0.34	fixed	fixed	0.38	0.27
Propeller 3/4 % Span Location	-	-	fixed	fixed	1.00	0.82
Propeller 5/6 % Span Location	-	-	fixed	fixed	0.38	0.27
Propeller 7/8 % Span Location	-	-	fixed	fixed	1.00	0.82
M.W. Span	11.40	13.00	11.40	12.30	9.60	10.52
M.W. Taper	0.70	0.54	0.70	0.85	1.00	0.82
M.W. Section 1 Twist (deg)	3.00	3.16	3.00	2.98	4.00	3.82
M.W. Section 2 Twist (deg)	2.75	2.59	2.75	2.73	3.00	3.18
M.W. Section 3 Twist (deg)	2.50	2.41	2.50	2.26	2.00	1.82
M.W. Section 4 Twist (deg)	2.25	1.84	2.25	2.85	1.00	1.18
M.W. Section 5 Twist (deg)	2.00	1.16	2.00	1.01	0.00	-0.18
T.W. Span	-	-	-	-	9.60	10.4
T.W. Taper	-	-	-	-	1.00	0.82
T.W. Section 1 Twist (deg)	-	-	-	-	4.00	4.18
T.W. Section 2 Twist (deg)	-	-	-	-	3.00	2.82
T.W. Section 3 Twist (deg)	-	-	-	-	2.00	2.18
T.W. Section 4 Twist (deg)	-	-	-	-	1.00	0.82
T.W. Section 5 Twist (deg)	-	-	-	-	0.00	0.18

The second optimization was that of the GA-8P aircraft, possessing a more distributed propulsion architecture along the span of the wing. Even before optimization, the 30% decrease in total energy of the baseline configuration compared to the twin-propeller GP-2P aircraft underscores the benefits of greater aero-propulsive coupling and an increased lift from the propulsion network that increases dynamic pressure across the blown surfaces. As noted previously, the percent span locations of the propellers were held fixed for equal spacing between propellers. The optimized result showed a 7.25% reduction in total energy consumption over the full mission profile. Additionally, it can be seen that the design conditions of the propeller are slightly higher than the baseline, but a decrease in tip radius from 0.58 to 0.55m occurs due to a violation of the tip Mach constraint of the initial design point. This optimized blade design has a higher solidity and operates at lower tip speeds favourable for low noise. The optimized main wing possesses a slightly higher aspect ratio and washout, but lower taper than the original wing, leading to a 2% increase in span efficiency in cruise. The increased tip chord increases the lift produced near the wingtips of the aircraft and also helps to delay the onset of stall.

*Indicates initial point violated a constraint.

In the final optimization of the TTW EVTOL aircraft, rotor blades were designed to meet both the demands of hover and vertical flight at low airspeeds as well as forward flight at higher speeds through lower throttle settings. Moreover, each segment of the mission outlined in Section VI for this aircraft is characterized not only by vehicle flight dynamics such as flight speed and altitude, but also the pitch command of the rotor blades, β_c. These rotor pitch commands documented in Table 4 of Appendix X.B are held fixed within the optimization routine in the present study. A 9.5% reduction in total battery energy consumption was achieved with rotors of 1.38m radius designed at operations conditions documented in the table above. Note that the originally identical tandem and main wings underwent different geometric transformations in the optimization, with the forward tandem wing having a greater root twist and overall washout than the aft main wing. The outermost rotors of the optimized tilt-wing configuration are also not positioned at the wingtip but rather around the 80% span location of the wing. With no propeller-on-propeller interaction modeled in this study, it is suspected that the configuration with the highest aero-propulsive efficiency is one in which rotor wakes are closely aligned to emulate a continuous zone of high dynamic pressure. That is, the optimizer will tend to reduce the distance between rotors as seen from the results above. The modeling of propeller-on-propeller interactions is the subject of future work.

IX. Conclusion

In this paper, we demonstrate full vehicle optimization for three aircraft with distributed electric propulsion architectures using a medium-fidelity approach. These aircraft are envisioned to operate shorter flight profiles with segments of comparable flight time, requiring the designer to weigh performance at off-design conditions. Optimizations were therefore formulated to capture cumulative aero-propulsive and system performance rather than performance at specific design points. Results indicate a 5-10% reduction in battery power consumption, suggesting the potential to increase vehicle range. Additionaly, the optimized distributed propeller case of the GA-8P showed significant energy reductions when compared to the optimized GA-2P configuration, highlighting the benefits of a DEP architecture.

Optimization of non-conventional aircraft is a challenge in that design variables can be discrete, for example the number of passengers or propellers, or they can be continuous as in the case of wingspan and rotor diameter. Following this study will be the examination of optimization algorithms suitable for handling such mixed-integer problems. Moreover, in future work we seek to address the difficulties encountered with numerical convergence, notably those issues arising from the propeller BEMT model and the battery network discharge model used to simulate the energy properties of the three aircraft. These shortcomings in robustness at the sub-component level develop convergence issues within the mission solver, placing a burden on the user to closely monitor the optimization progress. Future work will also address the rotor-on-rotor interactions that will have critical importance when considering acoustic impacts of these electric aircraft.

X. Appendix

A. Propeller Geometry for Validation Cases in Section IV

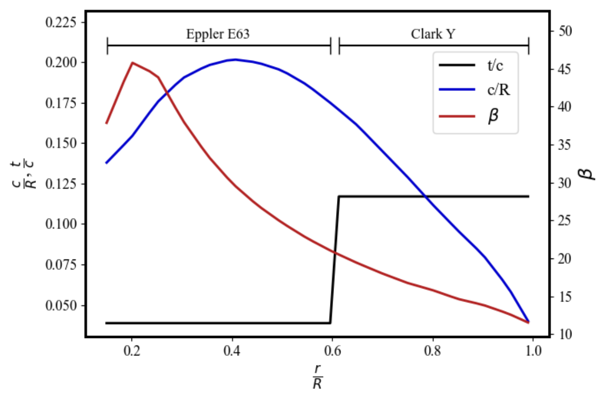

(a) APC 10x7 Thin Electric Propeller Geometry.

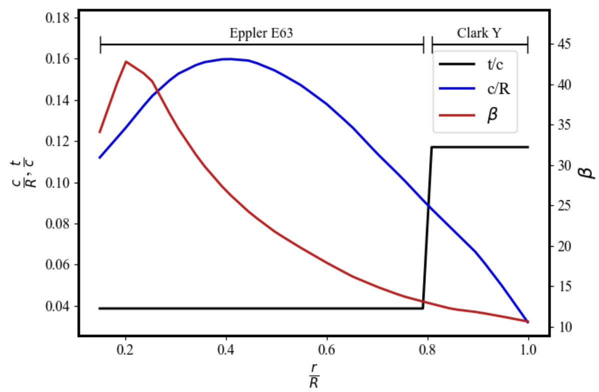

(b) APC 19x12 Thin Electric Propeller Geometry.

Fig. 13 Geometry of APC Propellers.

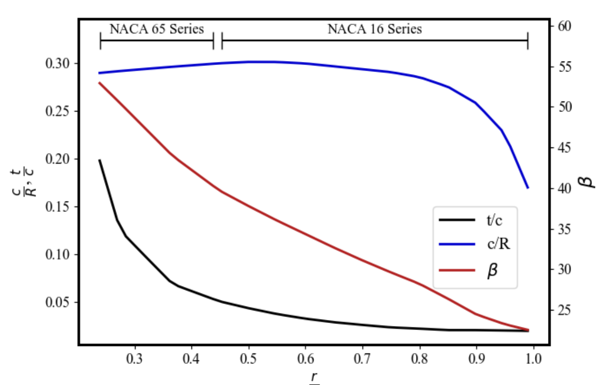

Fig. 14 SR2 Propeller Geometry, β_{75} = 29°.

B. Aircraft Flight Profile Segments

Documented in Tables 4 and 5 is the flight dynamics describing the full flight profile for the GA-2P, GA-8P and TTW aircraft. This includes the segment kinematics, airspeeds, climb rates and altitude at the beginning and end of each segment. The wing-mounted angle (WMA) and prescribed pitch command,β_c, for the respective segments of the tandem tilt-rotor are also provided below. For example, "90° x -5°" implies that wings and rotors are oriented 90° from the +ve x-axis which points out the nose of the fuselage, or parallel to the +ve z-axis, with a reduction in blade pitch of 5°.

Table 4 Flight Segment Kinematics in SUAVE

Segment	Symbol	Segment Kinematics
Approach Transition	AT	Constant-Acceleration-Constant-Angle-Linear-Climb
Baseleg	BL	Linear-Speed-Constant-Rate
Climb	CL	Linear-Speed-Constant-Rate
Climb Transition	CT	Constant-Acceleration-Constant-Angle-Linear-Climb
Cruise	CR	Constant-Speed-Constant-Altitude
Departure End of Runway	DER	Linear-Speed-Constant-Rate
Descent	D	Linear-Speed-Constant-Rate
Descent Transition	DT	Constant-Acceleration-Constant-Pitchrate-Constant-Altitude
Downleg	DL	Constant-Acceleration-Constant-Altitude
Final Approach	FA	Linear-Speed-Constant-Rate
Initial Climb Area	ICA	Linear-Speed-Constant-Rate
Landing	L	*Not Modeled*
Reverse Thrust	RT	*Not Modeled*
Takeoff	TO	*Not Modeled*
Vertical Climb	VC	Vertical Ascent
Vertical Transition	VT	Constant-Acceleration-Constant-Pitchrate-Constant-Altitude
Vertical Descent	VD	Vertical Descent

Table 5 Flight Segment Parameterization

Flight Segment	**Initial Altitude (ft)**	**Final Altitude (ft)**	**Initial Speed (mph)**	**Final Speed (mph)**	**Climb Rate (min)**	**WMA (deg) $\times \beta_c$ (deg)**
			GA Aircraft			
TO	0	0	0	91	0	-
DER	0	50	91	100	600	-
ICA	50	500	100	110	600	-
CL	500	2500	110	175	500	-
CR	2500	2500	175	175	0	-
D	2500	1000	175	50	-300	-
DL	1000	1000	50	100	0	-
RCL	1000	1500	100	150	500	-
RCR	1500	1500	150	150	0	-
RD	1500	1000	150	135	-300	-
BL	1500	500	135	90	-300	-
FA	500	0	90	78	-300	-
L	0	0	78	50	0	-
RT	0	0	50	0	0	-
			EVTOL Aircraft)			
VC	0	40	0	3.4	300	90×-5
VT	40	40	3.4	55	0	45×3
CT No.1	40	100	55	85	500	15×5
CT No.2	100	100	85	125	0	15×5
CL	100	2500	125	175	500	0×16
CR	2500	2500	175	175	0	0×20
D	2500	100	175	125	-300	0×16
RCL	100	1000	125	150	500	0×16
RCR	1000	1000	150	150	0	0×20
RD	1000	100	150	125	-300	0×16
AT	100	40	125	55	-200	0×16
DT	40	40	55	3.4	*	25×10
VD	40	0	3.4	3.4	-300	90×-5

References

[1] Sinnige, T., Van Arnhem, N., Stokkermans, T. C., Eitelberg, G., and Veldhuis, L. L., “Wingtip-mounted propellers: Aerodynamic analysis of interaction effects and comparison with conventional layout,” *Journal of Aircraft*, Vol. 56, No. 1, 2019, pp. 295–312.

[2] Kroo, I., “Propeller Wing Integration for Minimum Induced Loss,” *Journal of Aircraft*, Vol. 23, No. 7, 1986.

[3] Miranda, L., and Brennan, J., “Aerodynamic effects of wingtip-mounted propellers and turbines,” *4th Applied Aerodynamics Conference*, 1986.

[4] Cho, J., and Cho, J., “Quasi-Steady Aerodynamics Steady Aerodynamics Analysis of Propeller-Wing Interaction,” *International Journal for Numerical Methods in Fluids*, 1999.

[5] Cho, J., and Williams, M. H., “Propeller-wing interaction using a frequency domain panel method,” *Journal of Aircraft*, Vol. 27, No. 3, 1990, pp. 196–203.

[6] Witkowski, D. P., Lee, A. K., and Sullivan, J. P., “Aerodynamic interaction between propellers and wings,” *Journal of Aircraft*, Vol. 26, No. 9, 1989, pp. 829–836.

[7] McVeigh, M., Gray, L., and Kisielowski, E., “Prediction of span loading of straight-wing/propeller combinations up to stall,” Vol. 2602, 1975.

[8] Stone, R. H., “Aerodynamic Modeling of the Wing-Propeller Interaction for a Tail-Sitter Unmanned Air Vehicle,” *Journal of Aircraft*, Vol. 45, No. 1, 2008, pp. 198–210.

[9] Veldhuis, L. L. M., “Propeller Wing Aerodynamic Interference,” Ph.D. thesis, Delft Univ. of Technology, Delft, The Netherlands, 2005.

[10] Gomariz-Sancha, A., Maina, M., and Peace, A. J., “Analysis of propeller-airframe interaction effects through a combined numerical simulation and wind-tunnel testing approach,” *53rd AIAA Aerospace Sciences Meeting*, 2015, p. 1026.

[11] Roosenboom, E. W., Stürmer, A., and Schröder, A., “Advanced experimental and numerical validation and analysis of propeller slipstream flows,” *Journal of Aircraft*, Vol. 47, No. 1, 2010, pp. 284–291.

[12] Dang, T., “Simulations of propeller/airframe interference effects using an Euler correction method,” *Journal of aircraft*, Vol. 26, No. 11, 1989, pp. 994–1001.

[13] Thom, A., and Duraisamy, K., “Computational Investigation of Unsteadiness in Propeller Wake–Wing Interactions,” *Journal of aircraft*, Vol. 50, No. 3, 2013, pp. 985–988.

[14] Whitfield, D., and Jameson, A., “Euler equation simulation of propeller-wing interaction in transonicflow,” *Journal of Aircraft*, Vol. 21, No. 11, 1984, pp. 835–839.

[15] Clarke, M., Botero, E., MacDonald, T., Erhard, R., Smart, J., and Alonso, J., “SUAVE 2.4.0,” , May 2021. doi:10.5281/zenodo.4784705, URL `https://doi.org/10.5281/zenodo.4784705`.

[16] Miranda, L. R., Elliot, R. D., and Baker, W. M., “A generalized vortex lattice method for subsonic and supersonic flow applications,” Tech. rep., NASA Langley Research Center, 1977.

[17] Katz, J., and Plotkin, A., *Low-speed aerodynamics*, Vol. 13, Cambridge university press, 2001.

[18] Bertin, J. J., and Smith, M. L., *Aerodynamics for engineers*, Vol. 5, Prentice Hall New Jersey, 1998.

[19] Drela, M., “XFOIL: An analysis and design system for low Reynolds number airfoils,” *Low Reynolds number aerodynamics*, Springer, 1989, pp. 1–12.

[20] Spera, D. A., “Models of Lift and Drag Coefficients of Stalled and Unstalled Airfoils in Wind Turbines and Wind Tunnels,” Tech. rep., NASA/CR-2008-215434, 2008.

[21] Patterson, M. D., and German, B., “Conceptual Design of Electric Aircraft with Distributed Propellers: Multidisciplinary Analysis Needs and Aerodynamic Modeling Development,” *52nd Aerospace Sciences Meeting*, 2014.

[22] Brandt, J. B., Deters, R. W., Ananda, G. K., Dantsker, O. D., and Selig, M. S., “UIUC Propeller Database,” *https://m-selig.ae.illinois.edu/props/propDB.html*, 2015.

[23] Stefko, G. L., and Jeracki, R. J., “Wind Tunnel Results of Advanced High Speed Propellers in the Takeoff, Climb, and Landing Operating Regimes.” *NASA Technical Memorandum*, 1985.

[24] Veldhuis, L. L. M., "Propeller Wing Aerodynamic Interference," , 2005.

[25] Jameson, A., "Analysis of Wing Slipstream Flow Interaction," *NASA Technical Report*, 1970.

[26] Lukaczyk, T., Wendorff, A. D., Botero, E., MacDonald, T., Momose, T., Variyar, A., Vegh, J. M., Colonno, M., Economon, T. D., Alonso, J. J., Orra, T. H., and Ilario da Silva, C., "SUAVE: An Open-Source Environment for Multi-Fidelity Conceptual Vehicle Design," *AIAA Aviation Forum*, 2015.

[27] Adkins, C. N., and Liebeck, R. H., "Design of optimum propellers," *Journal of Propulsion and Power*, Vol. 10, No. 5, 1994, pp. 676–682.

[28] Chauhan, S. S., and Martins, J. R., "Rans-based aerodynamic shape optimization of a wing considering propeller–wing interaction," *AIAA Scitech 2020 Forum*, Vol. 1 PartF, No. January, 2020, pp. 1–20.